Observation of van der Waals phonons in the single-layer cuprate (Bi, Pb)$_2$(Sr, La)$_2$CuO$_{6+\delta}$

Y. Y. Peng [●],[1,*] I. Boukahil,[2,3] K. Krongchon [●],[4] Q. Xiao,[1] A. A. Husain [●],[4,5] Sangjun Lee,[4] Q. Z. Li,[1]
A. Alatas [●],[6] A. H. Said,[6] H. T. Yan,[7] Y. Ding,[7] L. Zhao,[7] X. J. Zhou,[7] T. P. Devereaux,[2,8] L. K. Wagner [●],[4]
C. D. Pemmaraju [●],[2] and P. Abbamonte[4,†]

[1]*International Center for Quantum Materials, School of Physics, Peking University, Beijing 100871, China*

[2]*Stanford Institute for Materials and Energy Sciences, SLAC National Accelerator Laboratory,*
2575 Sand Hill Road, Menlo Park, California 94025, USA

[3]*Department of Physics, Stanford University, Stanford, California 94305, USA*

[4]*Department of Physics and Materials Research Laboratory, University of Illinois, Urbana, Illinois 61801, USA*

[5]*Quantum Matter Institute and Department of Physics and Astronomy, University of British Columbia, Vancouver,*
British Columbia V6T 1Z4, Canada

[6]*Advanced Photon Source, Argonne National Laboratory, Argonne, Illinois 60439, USA*

[7]*Beijing National Laboratory for Condensed Matter Physics, Institute of Physics, Chinese Academy of Sciences, Beijing 100190, China*

[8]*Department of Materials Science and Engineering, Stanford University, Stanford, California 94305, USA*

Interlayer van der Waals (vdW) coupling is generic in two-dimensional materials such as graphene and transition-metal dichalcogenides, which can induce very low-energy phonon modes. Using high-resolution inelastic hard x-ray scattering, we uncover the ultralow energy phonon mode along the Cu-O bond direction in the high-T_c cuprate (Bi,Pb)$_2$(Sr,La)$_2$CuO$_{6+\delta}$ (Bi2201). The energy and full-width half-maximum (FWHM) of these modes are independent of temperature, while their intensity decreases with doping in accordance with an increasing c-axis lattice parameter. We compare the experimental results to first-principles density functional theory simulations and identify the observed mode as a van der Waals phonon, which arises from the shear motion of the adjacent Bi-O layers. This shows that Bi-based cuprate has vibrational properties similar to graphene and transition-metal dichalcogenides, which can be exploited to engineer novel heterostructures.

I. INTRODUCTION

Two-dimensional (2D) materials, such as graphene, transition-metal dichalcogenides (TMDs) and strongly correlated materials such as iron chalcogenides and cuprates [1] are held together by van der Waals (vdW) forces between different layers. These materials have attracted intensive interest due to a wealth of electronic properties and excellent mechanical properties, spanning from insulators, semiconductors, and metals, to superconductors [2–4]. More intriguingly, due to the weak interlayer vdW forces, one can create many exotic heterostructures by control of individual layers, such as twisted bilayer graphene [5], which exhibits superconductivity and other strongly correlated states, such as Mott-like insulator states [5], charge order [6], and strange metal state [7,8]. Therefore, vdW materials provide a platform to study numerous exotic physical phenomena and show great promise for applications such as optoelectronics, spintronics, and valleytronics [1,9].

The Bi-based cuprate family is one of the most studied materials among cuprates. Due to the weak vdW interaction within the adjacent Bi-O layers, it can be easily cleaved to get a clean and smooth surface, being widely studied by

many surface-sensitive technologies, such as angle-resolved photoemission spectroscopy (ARPES) and scanning tunneling microscopy (STM) [10,11]. There is a rich set of phases in cuprates such as Mott insulator, superconductor, pseudogap, and charge order [4]. Among them, charge order (CO) is considered a generic feature in high-T_c cuprates, while important questions remain about the extent to which the charge order influences lattice and charge degrees of freedom. These questions are intimately connected to the origin of CO and its relation to superconductivity. Due to the modulation of electron density, CO is typically associated with a lattice distortion if the electron-phonon coupling is strong enough. Indeed, due to the presence of CO, some phonon anomalies including energy softening and width broadening have been observed at CO wave vector for acoustic and optical phonons in YBa$_2$Cu$_3$O$_6$ (YBCO), (La,Ba)$_2$CuO$_4$ (LBCO), Bi$_2$Sr$_2$CaCu$_2$O$_8$ (Bi2212), and Bi$_2$Sr$_2$LaCuO$_{6+\delta}$ (Bi2201) [12–17], indicating the importance of lattice dynamics for electronic properties in cuprates.

In the present work, by using high-resolution inelastic hard x-ray scattering (IXS) [18,19] we studied the low-energy phonons in single-layer cuprate (Bi,Pb)$_2$(Sr,La)$_2$CuO$_{6+\delta}$ (Bi2201) as a function of momentum, temperature, and doping. We observed the low-energy phonons (∼4 meV) originating from the interlayer van der Waals interactions (vdW phonons) in cuprates. The experimental phonon energies agree well with first-principles density functional theory

*yingying.peng@pku.edu.cn

†abbamont@illinois.edu
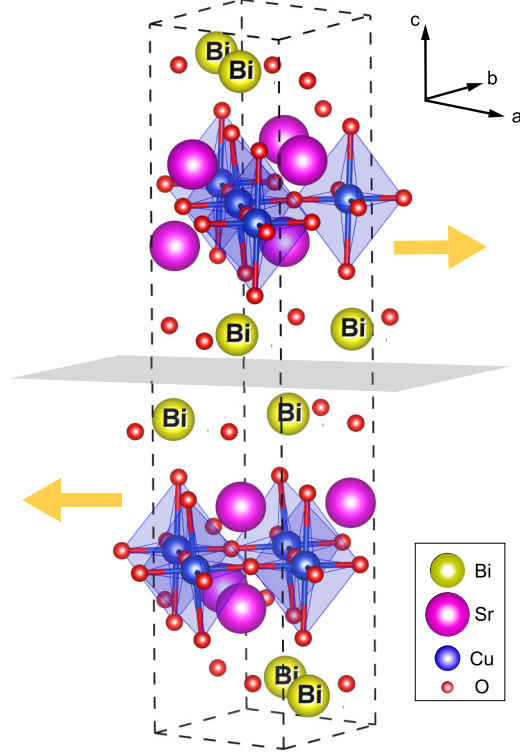
FIG. 1. Bi2201 crystal structure. The unit cell parameters are $a \simeq$ 5.436 Å, $b \simeq$ 5.502 Å, $c \simeq$ 23.91 Å. The orange arrows indicate the shear motions within the Bi-O layers discussed in the text.

(DFT) calculations [20,21]. Our results demonstrate that Bi-based cuprates have a similar interlayer vibration property as other 2D materials such as graphene and TMDs, where low-energy interlayer shear and breathing modes ($\sim$2–5 meV) have been observed [22,23]. The linewidth broadening of the low-energy phonon only occurs in underdoped Bi2201, where it persists up to 300 K. This behavior differs from the previous IXS results of double-layer Bi2212, which found low-energy phonon width broadening in both underdoped and overdoped samples [14]. This shows that the low-energy phonon broadening in Bi-based cuprates depends on the material-specific details, suggesting an origin in phonon hybridization rather than charge ordering.

II. METHODS

A. IXS experiment

We studied three doping levels of (Bi,Pb)$_2$(Sr,La)$_2$CuO$_{6+\delta}$ (Bi2201) as indicated in Fig. 2(a): antiferromagnetic (AF, $p \simeq$ 0.03), underdoped with T_c = 17 K (UD17K, $p \simeq$ 0.12) and overdoped with T_c = 11 K (OD11K, $p \simeq$ 0.21). Underdoping was achieved via partial substitution of Sr with La to form Bi$_2$(Sr,La)$_2$CuO$_{6+\delta}$, while heavy overdoping was achieved via partial substitution of Bi with Pb to form (Bi,Pb)$_2$Sr$_2$CuO$_{6+\delta}$. The sample growth and characterization methods have been reported previously [10,24]. The IXS experiments were performed with HERIX spectrometer at Sector 30 of Advanced Photon Source at Argonne National Laboratory [25,26]. The incident x-ray energy is 23.724 keV with an energy resolution

TABLE I. Comparison of experimental and calculated lattice constants (in Å) for hole-doped Bi2201 systems. Calculated constants are obtained with the rev-vdW-DF2 functionals, except for 0%, which is also obtained by the PBE0 functional.

	Experiment			Calculated			
	AF	UD15K	OD11K	0% (PBE0)	0%	12%	20%
a	5.436	5.4	5.4	5.182	5.289	5.268	5.258
b	5.502	5.445	5.308	5.347	5.362	5.375	5.366
c	23.91	24.34	24.56	24.47	24.857	24.945	24.961

of $\Delta E \sim$ 1.4 meV. The samples were glued to a sample holder inside a closed-cycle cryostat on a four-circle goniometer. The Bi2201 crystal structure is shown in Fig. 1 plotted using VESTA software [27], where vdW forces hold the adjacent Bi-O layers together. The reciprocal lattice units for Bi2201 throughout this paper are based on the orthorhombic cell convention [28]. The IXS experiments were performed along both longitudinal direction and traverse direction around (2,2,0) as shown in Fig. 2(b) using transmission geometry. The lattice constants of Bi2201 determined from IXS measurements at 300 K are shown in Table I.

III. EXPERIMENTAL RESULTS

A. Observation of van der Waals modes

We performed our IXS experiment around the orthorhombic (2, 2, 0) peak since it is one of the strongest accessible Bragg reflections. It is interesting to investigate if there is any phonon anomaly relating to CDW. Considering that CDW has been observed maximum at T_c [29] and persists up to high temperatures as charge fluctuations [30], our IXS measurements on UD17K were performed at two different temperatures of 17 K and 300 K. The momentum-energy intensity color maps are shown in Figs. 2(c) and 2(d), respectively. Here, the positive energy corresponds to photon energy loss, while the negative energy corresponds to photon energy gain. No charge ordering peak is detected in the vicinity of (2.25, 2.25, 0) within the elastic peak, a phenomenon previously reported through soft x-ray resonant scattering at the Cu L_3 edge [11,31]. This finding agrees with prior IXS results for Bi2212 [14] but contrasts with the quasielastic peak identified in YBCO [12]. The distinction may stem from the relatively weaker and shorter-ranged charge modulations in Bi-based cuprates. We also observed symmetric Stokes and anti-Stokes components at 300 K due to phonon creation and annihilation, while only the Stokes phonons remain at 17 K due to the Bose factor.

The IXS spectra at varying reciprocal momenta for 300 K and 17 K are shown in Figs. 2(e) and 2(f), respectively. The spectra are shifted vertically for clarity. The spectra are composed of the elastic component centered at zero energy and the inelastic components due to Stokes and anti-Stokes scattering from phonons. The elastic component is fitted with an intensity-scaled resolution function. The phonon excitations were fitted to the resolution-convolved Lorentz functions with the Bose factor correction. The fittings for one selected IXS spectrum are shown in Fig. 8 in the Ap-
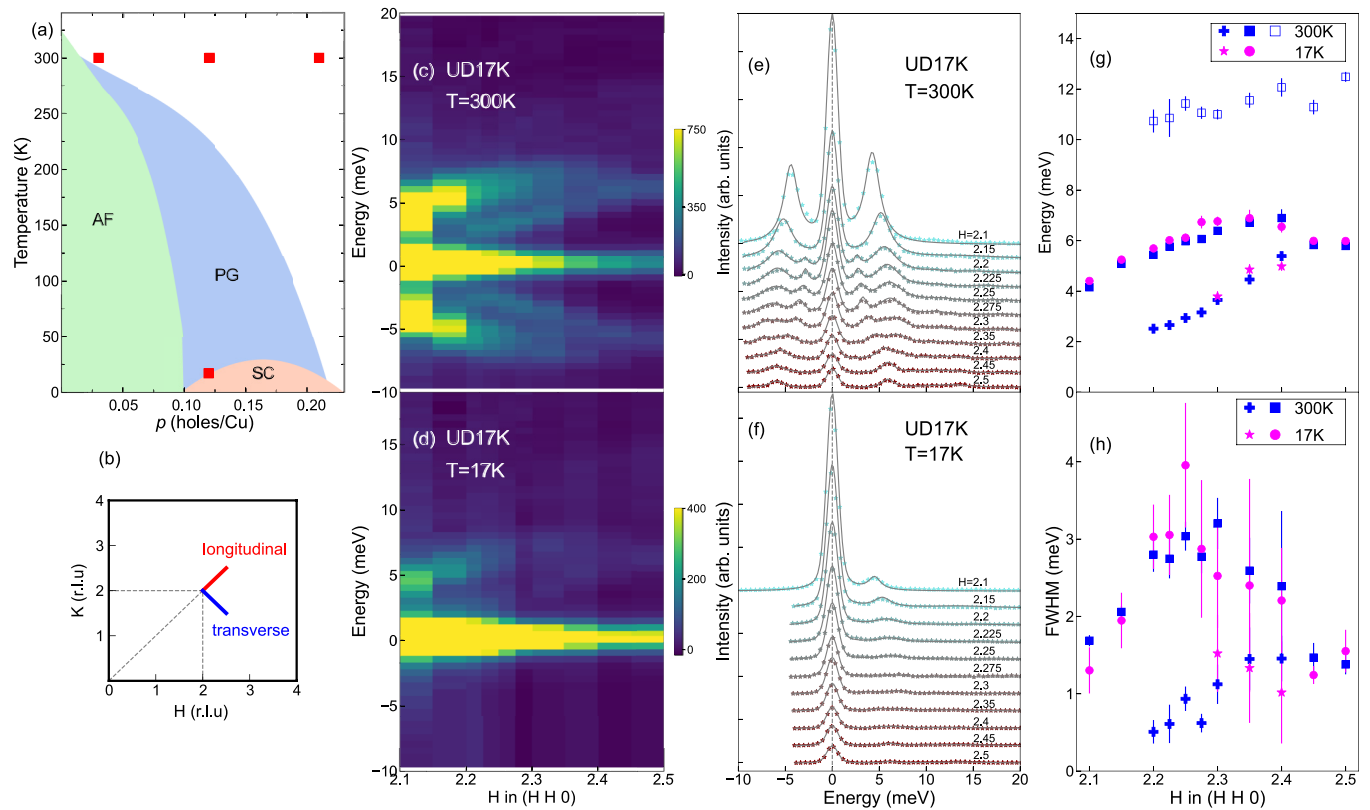
FIG. 2. (a) Phase diagram of Bi2201, where the green shaded area indicates the antiferromagnetic (AF) region, the blue shaded area indicates pseudogap (PG) region, and the orange region indicates superconductivity (SC) region. The red square markers indicate our measurements. (b) Schematic plot of momentum space. The red line and blue line indicate our measurements along a longitudinal direction and transverse direction, respectively. (c), (d) Temperature dependence for UD17K Bi2201. Low-energy longitudinal phonon dispersions along the (H H 0) direction at 300 K and 17 K, respectively. (e), (f) Momentum dependence of the IXS spectra (markers) along the (H H 0) direction and the corresponding fittings (lines) overlapped on top. (g), (h) Momentum evolution of fitting parameters for phonon dispersion and phonon intrinsic FWHM at 17 K (magenta markers) and 300 K (blue markers). Note that width values do not include the experimental energy resolution, which has been accounted for by the resolution convolution. The hollow markers indicate the higher-energy modes, while the filled markers indicate the low-energy modes with details in the text.

pendix. The results of these fits for phonon dispersions and the intrinsic full-width at half-maximum (FWHM) are displayed in Figs. 2(g) and 2(h). The phonon dispersions and FWHM are similar at the two temperatures, which do not follow the temperature-dependent changes observed in the CDW [11,29–31].We can clearly identify three phonon modes from the phonon dispersions. The two higher-energy modes with energy range ∼10–12 meV and ∼4–7 meV are similar to those observed in bilayer Bi2212, which were assigned to the longitudinal acoustic mode and one low-energy optical mode [14].

The lowest-energy phonon, with an energy range from 2–5 meV, falls below the range for an acoustic phonon, which typically disperses up to around 16 meV [32]. Moreover, it does not go to zero at (2,2,0) considering its curvature. Instead, this ultra-low-energy phonon closely resembles the very low-energy vdW modes (∼2–5 meV) observed in a series of layered materials, such as few-layer graphene [22] and TMD materials [23]. We illustrate below that this ultralow energy phonon is the vdW mode of Bi2201, arising from the interlayer vdW restoring force. This force induces in-plane shear motions between Bi-O layers, with half unit-cell displacing together. We did not observe phonon softening at the

expected charge order wave vector (2.25, 2.25, 0) at 300 K [see Fig. 2(g)]. At 17 K, we were unable to extract the energy and width for the vdW phonon below (2.275, 2.275, 0) due to the weakened phonon intensity, making reliable fitting challenging. Therefore, we cannot determine if the vdW phonon mode softens at T_c.

We have observed a width broadening of ∼3 meV for the low-energy optical mode around (2.25, 2.25, 0) [see Fig. 2(h)], a phenomenon also noted at a similar momentum in Bi2212 [14]. It has been proposed that the broadening of phonon width is due to the simultaneous measurement of multiple phonons close in energy to each other, thus the amplitude of the eigenvector changes throughout the zone and shows up prominently at (2.25, 2.25, 0) [14]. Notably, this broadening effect is absent in Pb-substitution underdoped Bi2201 samples where Pb suppresses the well-known structural incommensurate supermodulation [33]. This suggests that the phonon dispersions and widths are highly sensitive to the details of the crystal structure rather than the presence of charge order. It is worth noting that the FWHM of the vdW mode is only ∼1 meV after deconvolving the energy resolution. Both phonon dispersions and FWHMs exhibit no obvious change at 17 K and 300 K.
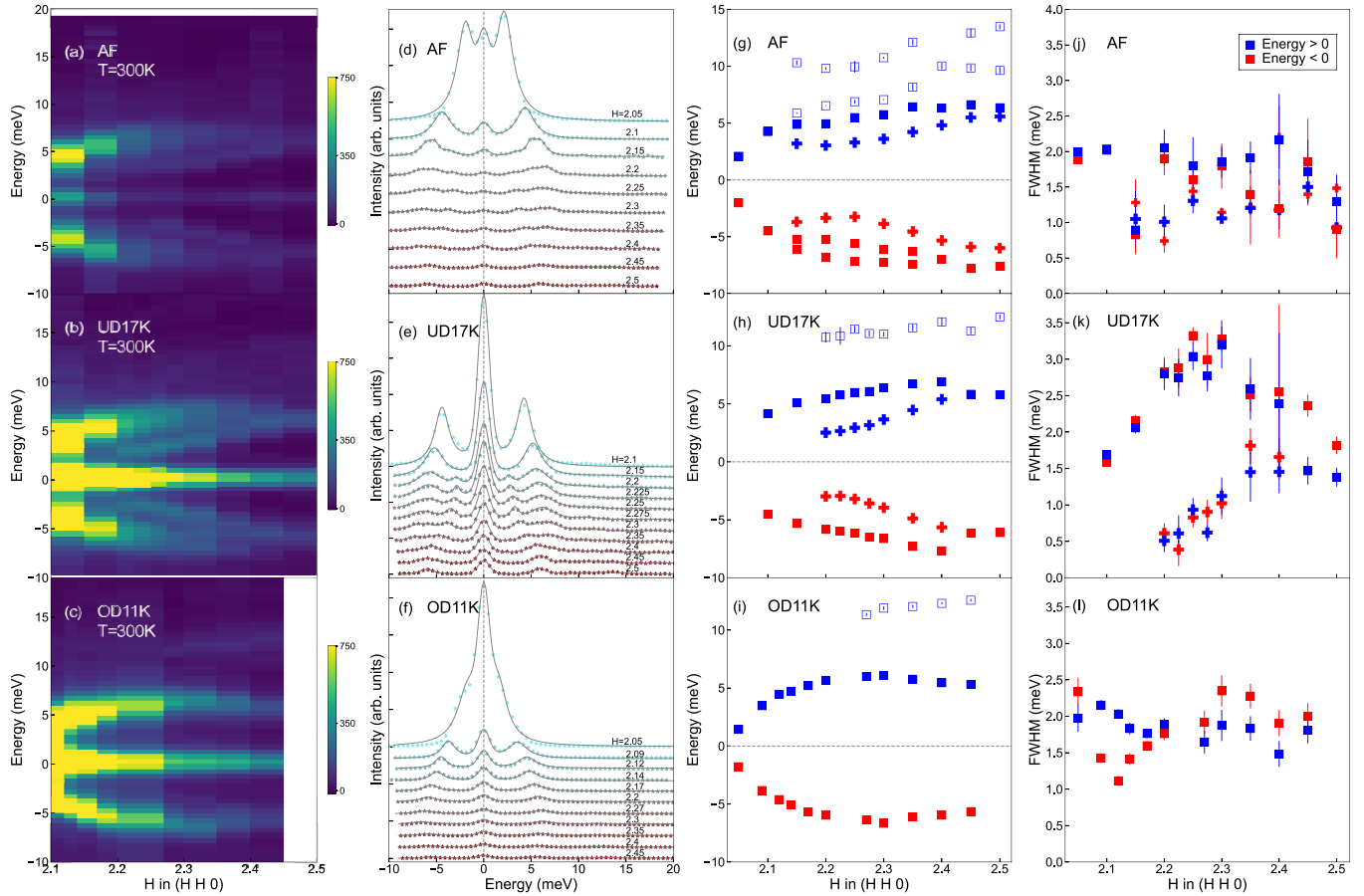
FIG. 3. Doping dependence of longitudinal phonons for Bi2201 at 300 K. Low-energy longitudinal phonon dispersions along the (H H 0) direction for AF (a), UD17K (b), and OD11K (c). (d)–(f) Momentum dependence of the IXS spectra (markers) along the (H H 0) direction and the corresponding fittings (lines) overlapped on top. (g)–(i) Momentum evolution of fitting parameters for phonon dispersion for AF, UD17K and OD11K, respectively. (j)–(l) The corresponding intrinsic FWHM evolution of phonon with filled square markers in (g)–(i). Note that width values do not include the experimental energy resolution, which has been accounted for by the resolution convolution. The hollow markers indicate the higher-energy modes, while the filled markers indicate the low-energy modes with details in the text. The Stokes and anti-Stokes components are indicated as blue and red markers, respectively.

B. Doping dependence

We now explore the doping dependence of low-energy phonons in Bi2201. First, we studied the longitudinal phonons (LA) of Bi2201 at 300 K, as shown in Fig. 3. The Stokes and anti-Stokes phonons show very symmetric behaviors, which can be noticed clearly in Figs. 3(a)–3(c). One additional phonon branch ($\sim$5–10 meV) can be identified in the AF sample [Fig. 3(g)] compared to UD17K [Fig. 3(h)]. From our fitted phonon dispersion in Figs. 3(g)–3(h), we notice a change of slope in the low-energy phonon branches between AF and UD17K samples. The vdW phonon of UD17K disperses to lower energy near (2.2, 2.2, 0). This is due to the change of interlayer vdW coupling between Bi-O layers as a function of doping as discussed later. The low-energy vdW mode is obvious in AF and UD17K, whereas its intensity fades in OD11K. We notice that the c-axis lattice parameter increases with doping (Table I). This indicates the interlayer coupling is influenced by the c-axis spacing, which is confirmed by the calculations shown below. We expect the vdW mode would persist in one unit-cell Bi-based

cuprates but having a smaller energy, akin to the layer dependence of shear modes reported in multilayer graphene [22], MoS_2 and WSe_2 [23]. This is anticipated by a decrease of restoring force with a decreasing number of layers [22]. The phonon FWHMs for the most intense branch and vdW mode are shown in Figs. 3(j)–3(l). The FWHMs from both Stokes (blue markers) and anti-Stokes (red markers) components agree well with each other. Interestingly, the phonon broadening at (2.25, 2.25, 0) for the low-energy optical mode only exists in UD17K and disappears in both AF and OD11K samples, highlighting its sensitivity to doping. Similar phonon broadening was observed in underdoped Bi2212, which was suggested relating to the intrinsic phonon-phonon hybridization [14].

We also display the transverse cuts taken along ($2 + \delta$, 2-δ, 0) direction for three dopings of Bi2201 at 300 K, which is shown in Fig. 4. The transverse branches appear at slightly lower energies than the longitudinal branches. The phonon FWHMs for the most intensive branch is shown in Figs. 4(j)–4(l). Clearly, there is no phonon width broadening for the
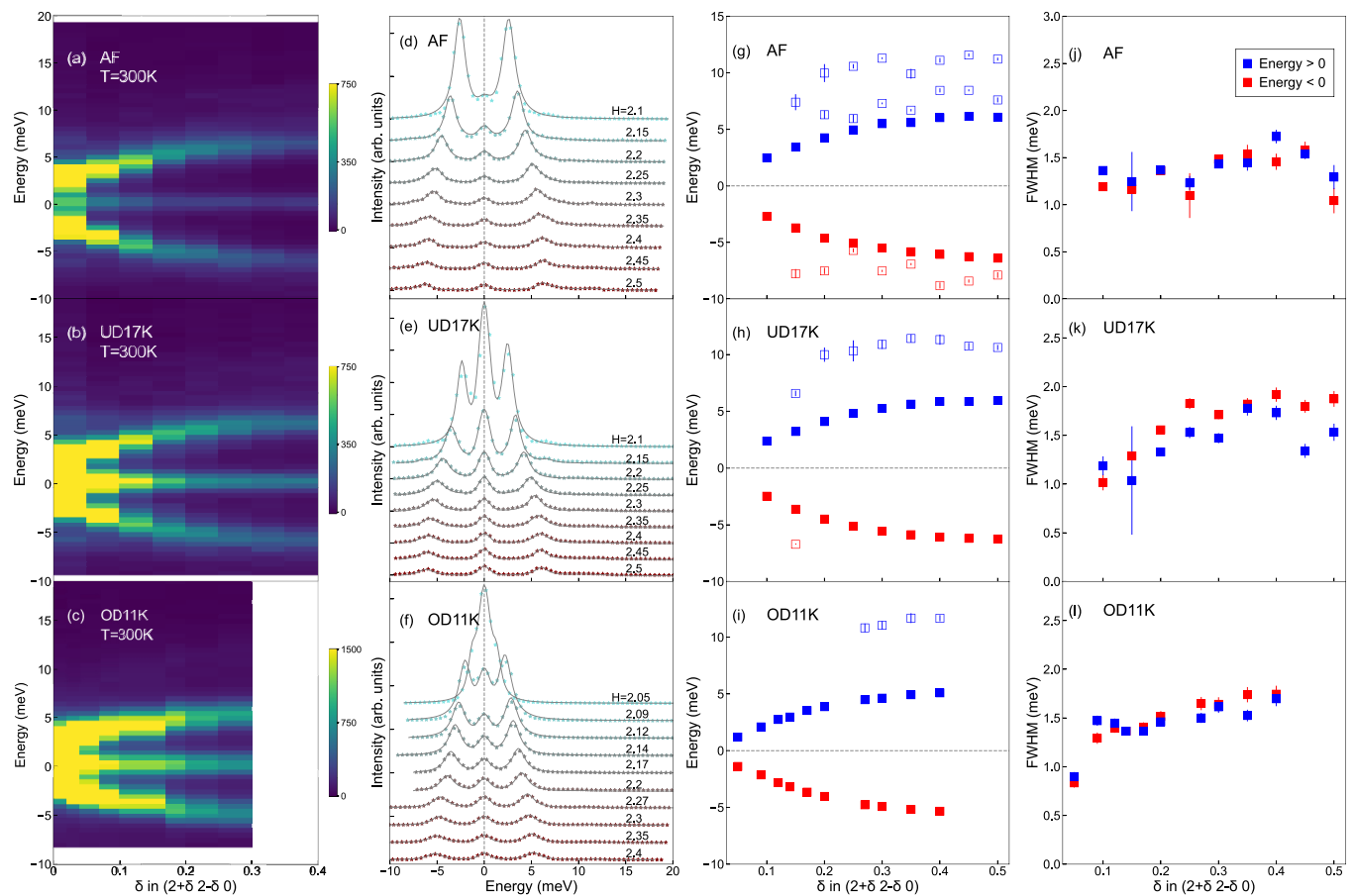
FIG. 4. Doping dependence of transverse phonons for Bi2201 at 300 K. Low-energy transverse phonon dispersions along the $(2 + \delta, 2-\delta, 0)$ direction for AF (a), UD17K (b), and OD11K (c). (d)–(f) Momentum dependence of the IXS spectra (markers) along the $(2 + \delta, 2-\delta, 0)$ direction and the corresponding fittings (lines) overlapped on top. Momentum evolution of fitting parameters for phonon dispersion (g)–(i) and phonon intrinsic FWHM (j)–(l) for AF, UD17K, and OD11K, respectively. Note that width values do not include the experimental energy resolution, which has been accounted for by the resolution convolution. The hollow markers indicate the higher-energy modes, while the filled markers indicate the low-energy modes with details in the text. The Stokes and anti-Stokes components are indicated as blue and red markers, respectively.

transverse branches as shown in Figs. 4(j)–4(l). Furthermore, the lowest-energy vdW mode is absent for all three doping levels in the transverse cuts [Figs. 4(g)–4(i)]. This observation may be related to the IXS cross sections, considering the polarization dependence of the IXS cross section on phonons, which is proportional to $(\vec{Q}.\vec{\epsilon})^2$ where $\vec{\epsilon}$ is the phonon eigenvector [34]. This suggests that the vdW mode is not IXS active in the transverse direction.

IV. THEORY RESULTS

The experimental observations presented in the previous section can be understood qualitatively on the basis of first-principles phonon simulations (see details of theory in the Appendix). A quantitative comparison is, however, hindered as the superstructure modulation of the Bi-O sublattice is not accounted for in the simulations. Regardless of the methodology employed to calculate the phonons, we find that (with an exception for a narrow regime of doping levels on the Bi-O zigzag bonding structure), models based on the approximate ORTH periodic unit cell predict unstable modes at wave vectors away from the zone boundary. Nevertheless, the modes

at the zone center, as well as band dispersions along certain high-symmetry directions in the BZ, are well behaved and are analyzed here.

First, we analyze the character of the low-energy vdW modes using the PBE0 functional. The calculated phonon frequencies are reported in Table II and plotted along with the IXS and rev-vdW-DF2 results in Fig. 5. The labels Γ and M represent phonon modes at $\vec{q} = (2, 2, 0)$ and $(2.5, 2.5, 0)$, respectively. The figure shows low-energy optical and acoustic branches mixing together into four nearly degenerate phonons at the Brillouin zone boundary. The frequencies from PBE0 are in good agreement with the rev-vdW-DF2, except for the two additional low-energy bands at 1.74 meV and 1.75 meV, which are discussed in the following paragraph. The phonon eigenvectors are displayed in Fig. 6, with the top row being the top view and the bottom row being the side view. From the diagram, the M1 and M2 modes are associated with the rotation of the Bi planes, while the M3, M4, Γ4, and Γ5 modes are associated with plane shearing. All low-energy modes are due to the weakly bound cleavage plane. From the calculations, we ascertain that vdW modes are primarily associated with a- and b-direction motions of the Bi atoms

TABLE II. Phonon frequencies from different functionals in meV. Values obtained from the rev-vdW-DF2 functional are using the XY structure.

$\bar{q}$	PBE0	PBE	rev-vdW-DF2
$\Gamma 4$	4.233	4.897	0.421
$\Gamma 5$	4.272	5.129	0.423
$\Gamma 6$	5.489	5.698	0.945
$\Gamma 7$	6.297	6.776	0.977
$\Gamma 8$	7.667	7.330	0.979
$\Gamma 9$	8.572	8.073	1.111
M5	9.005	9.009	NA
M6	9.258	9.714	NA
M7	9.438	9.877	NA
M8	9.477	10.938	NA
M9	9.957	11.517	NA
$\Gamma 10$	10.903	10.068	1.114
M10	11.746	11.771	NA
M11	12.024	12.236	NA
M12	12.045	12.318	NA
$\Gamma 11$	12.152	10.463	1.647
M13	12.396	12.521	NA
M14	12.481	12.629	NA
$\Gamma 12$	12.712	10.836	1.660

in adjacent Bi-O layers, explaining why the vdW functional obtains different frequencies from the hybrid functional.

Based on structure optimizations using the vdW functional, we find that although the Bi-O zigzag bonding variation predicts a lower ground-state energy compared to the XY variation (on the order of 0.1 eV per unit cell), both structures predict unstable phonon modes away from the zone boundary when undoped. Such instabilities cannot be eliminated by
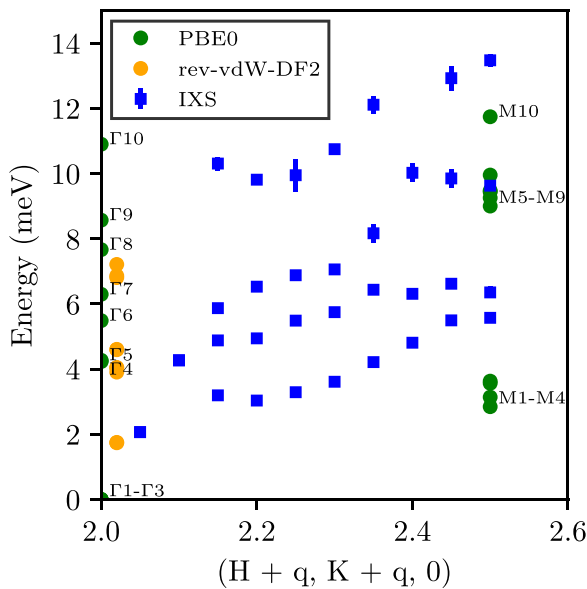
FIG. 5. Theoretical and experimental phonon frequencies for Bi2201. The theoretical phonons were computed using DFT in the PBE0 approximation. We associate the M1–M4 modes with the modes seen experimentally at the Brillouin zone boundary, and the $\Gamma 4$ and $\Gamma 5$ modes to the optical modes at Γ.

considering energy-lowering distortions that fit within small periodic cells. However, in the Bi-O zigzag structure within the range of 6%–14% hole doping, no unstable modes are seen, suggesting that this structure is at least a local minimum in the PES over this doping range. Further, our modified ORTH XY structure experiences an antiferromagnetic-to-ferromagnetic phase transition at 26% hole doping. This is in good agreement with the two-dimensional ferromagnetic fluctuations observed in overdoped Bi2201, where the magnetic ground state changes from antiferromagnetic to ferromagnetic with increasing doping [35]. However, we simplify our qualitative analysis by including only the antiferromagnetic configurations up to 20% hole doping.

Figure 7 shows the simulated IXS and calculated dispersions of three hole doping levels considered within the frozen-phonon method and the rev-vdW-DF2 functional on the modified XY ORTH structure. Both the XY and zigzag configurations predict the vdW phonon modes measured experimentally but the latter structure exhibits very low simulated IXS intensity (phonon dispersions and simulated IXS are shown in the Appendix). Because the incommensurate modulations in the true Bi2201 system allow for numerous potential Bi-O bonding configurations to coexist [36], we hypothesize that the *a*- and *b*-direction Bi-O dimerization motif similar to the one present in our XY structure is responsible for the experimentally measured vdW IXS intensity. Therefore, for comparison with experimental IXS results, Fig. 7 is presented with the XY structure. Additionally, we note that the dispersions and intensities for the XY structure are presented along the (200) high symmetry direction of Bi2201 whereas experimental observations are made along the (220) direction. As before, this choice is made to reveal qualitative trends while avoiding complications arising from the incommensurate superstructure that is not modeled.

From the calculated volume studies of our doped systems (Table I) we see a similar trend with experimental observations, namely that the *c*-lattice constant increases with increasing doping level (from $c = 24.857$ Å in the undoped system to about $c = 24.961$ Å in the maximally doped system). Our calculation shows that the vdW mode gets lower near (2.2, 2.2, 0) with increasing doping due to the elongation in the *c* axis. As alluded to before, we expect this increase of the *c*-axis dimension to weaken the interlayer vdW coupling between Bi-O layers in the Bi2201 cell, causing a reduction in vdW phonon mode energy. Indeed, the modes marked by white arrows in Figs. 7(b), 7(c) show this softening between 12% and 20% doped systems. We note that the same mode is not IXS active in the undoped system [Fig. 7(a)]. The hybridization between different modes is modulated across the doping regime causing the relative intensities of modes to vary. A similar volume study performed on the Bi-O zigzag structure (results shown in the Appendix) also predicts a *c*-lattice expansion (from $c = 24.5535$ Å in the minimally doped system to about $c = 24.5571$ Å in the maximally doped system). The lesser degree of expansion compared to experimental observations supports our hypothesis that the experimental system exhibits more *a*- and *b*-direction Bi-O dimerization motifs than the zigzag chain bonding. We note that vdW phonons were seen in the overdoped sample in the DFT+U simulation. This is associated with a simplified
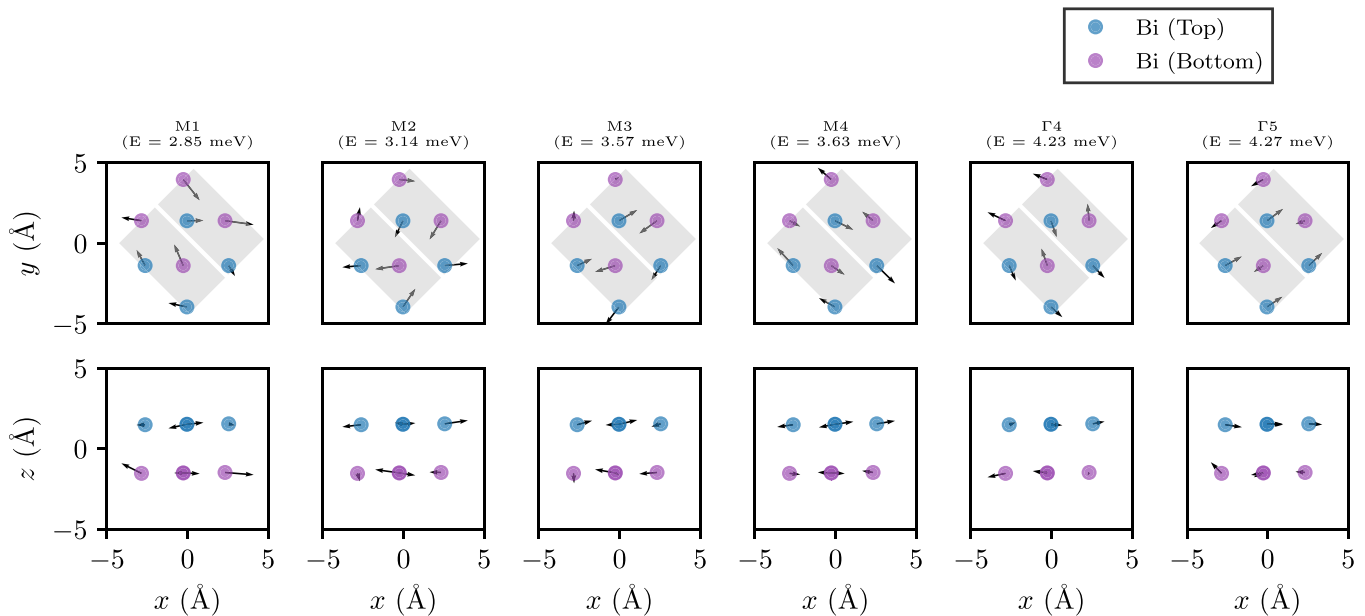
FIG. 6. Phonon eigenvectors from DFT (PBE0) calculations. Oxygen atoms are not included in the plots to clearly visualize the displacement of Bi atoms. Each column displays a phonon mode, with the top layer showing the top-down view and the bottom layer showing the side view.

model of the lattice structure and an unrealistic description of the overdoped magnetic ordering. Our simulations constrain the magnetic ordering in the overdoped region to be antiferromagnetic, which is unrealistic. So, the IXS intensity for VdW modes observed in the overdoped simulations cannot be directly compared to the experiment.

V. DISCUSSION

The vdW phonons in cuprates arise from vdW forces between stacked two-dimensional building blocks. Among the cuprate family, Bi-based cuprates are bound together by van der Waals forces between BiO layers. Consequently, vdW modes are anticipated in all Bi-based cuprates. An earlier inelastic x-ray scattering (IXS) study on bilayer Bi2212 revealed comparable low-energy phonons in the range of 2–5 meV, while leaving the discussion open regarding their origin [33]. In contrast, higher-energy phonon modes exceeding 5 meV are observed in other cuprates such as YBCO [12] and LBCO [13]. This disparity is attributed to the absence of van der Waals bonding between layers in these materials, unlike the Bi-based cuprates.

While vdW phonons may not directly influence the strongly correlated effects in cuprates, such as charge order, pseudogap, and superconductivity, their presence underscores a similarity between cuprates and TMD materials. This similarity proves valuable for using cuprates in the design of novel 2D materials. For instance, by employing out-of-plane alignments such as interlayer twisting and vertical displacements, Bi-based cuprates can be utilized to engineer innovative heterostructures akin to graphene and TMDs. A proposal suggests that high-temperature topological superconductivity can be achieved in twisted Bi2212 by mechanically exfoliating and controlling the twisted angles around 45° [37].

Additionally, stacking and twisting ultrathin Bi2212 crystals enable the measurement of Josephson junctions along the *c* direction, a technique applied to determine the pairing symmetry of cuprates [38,39].

VI. CONCLUSION

In summary, our high-resolution inelastic x-ray scattering study has mapped the low-energy phonon dispersions and unveiled the presence of van der Waals modes in cuprate Bi2201. We also conducted comprehensive first-principles density functional theory simulations specifically targeting low-energy phonons in Bi2201. The synergy between experimental and theoretical findings is striking, with qualitative similarities observed in both the phonon energy scale and dispersions. Our theoretical analysis determines the vdW character of the low-energy phonons in Bi2201, involving shear motions along the cleavage plane. Intriguingly, these vdW modes exhibit softening with increasing doping, accompanied by a concurrent expansion of the *c*-axis lattice. Our results establish the generality of vdW modes in layered materials characterized by interlayer vdW interactions. This includes complex systems such as doped copper oxides, showcasing the versatility of vdW modes even in chemically intricate environments. The understanding gained from our study opens avenues for harnessing the unique properties of vdW interactions in the design and development of novel electronic devices, extending the potential applications of Bi2201 and similar materials in the domain of two-dimensional materials and electronics.
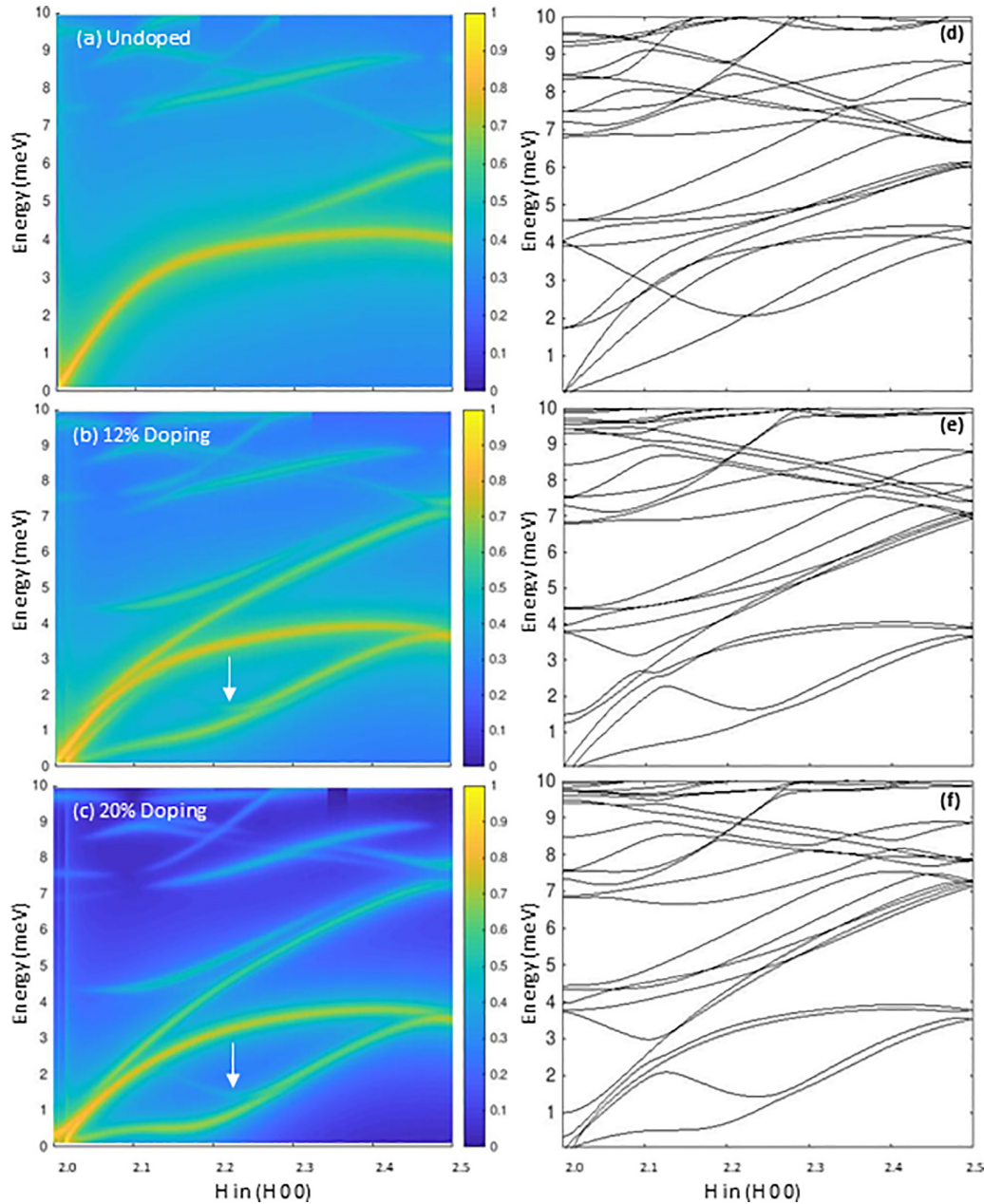
FIG. 7. Theoretical doping dependence of phonons for Bi2201 using the rev-vdW-DF2 functional on the XY structure. Simulated IXS spectra along the (H 0 0) direction for (a) 0% doping, (b) 12% doping, and (c) 20% doping. (d)–(f) Calculated phonon dispersions for 0%, 12%, and 20% doping, respectively. Intensities have been normalized and plotted on a logarithmic scale for clarity. All systems are in the antiferromagnetic state.

FIG. 8. Example fit of one selected IXS spectrum of UD17K taken at 300 K at $Q = (2.25, 2.25, 0)$. The dashed red line represents the resolution function profile with 1.4-meV FWHM. The dashed magenta and green lines represent the results of fits to the inelastic intensity. The solid red line is the sum of these contributions.

APPENDIX A: IXS DATA FITTING

The experimental data were fitted using Lorentz functions, convoluted with the experimental resolution, as shown in Fig. 8. The position and linewidth of the phonons reported in the paper are deconvoluted from the resolution.

APPENDIX B: THEORY

Low-energy vibrational properties of Bi2201 associated with the shear motions of the Bi-O planes were analyzed using phonon calculations based on ground-state DFT. As noted previously by a number of authors, the observed geometry of Bi2201 crystals exhibits an incommensurate superstructure and is not amenable to a description based on small periodically repeating unit cells [40,41]. In particular, the superstructure involves incommensurate modulations of the Bi-O sublattice, which manifest as a variety of different Bi-O bonding configurations between and within the sublattices [36]. For analyzing the electronic properties of Bi2201, such as the Fermi surface [41], theoretical methods, therefore, employed an approximate periodic structure based on the $\sqrt{2} \times \sqrt{2}$ orthorhombic (ORTH) cell determined by Torardi *et al.* [42], which is similar to the schematic structure shown in Fig 1. Simulations of phonon properties in this study

are also based on periodic supercells constructed from the approximate ORTH structure. The optimized geometries of such small periodic cells, however, do not correspond to the global minimum structure of Bi2201 (which is incommensurate) but instead represent either nearby local minima or alternately saddle points on the high-dimensional potential energy surface (PES). In order to extract a consistent and useful qualitative description of Bi2201 phonons from periodic cell models we carried out different sets of simulations. First, in order to visualize atomic displacements associated with both zone center and zone boundary normal modes of interest, we carried out phonon calculations using the CRYSTAL17 package [43,44]. These calculations also employed both hybrid and semilocal exchange-correlation (XC) functionals to assess the robustness of the description with respect to the choice of XC functional. Next, in order to map out phonon dispersions across the Brillouin zone and make contact with experimental IXS spectra, we performed frozen phonon simulations with the VASP [45] and PHONOPY [46,47] codes employing dispersion correct vdW DFT functionals [48]. Numerical parameters characterizing both sets of simulations are listed in the following.

Calculations with the CRYSTAL17 package [43,44] carried out geometry optimizations on undoped Bi2201 with the ORTH structure using both semilocal PBE [49] and nonlocal hybrid PBE0 [50] XC functionals. The hybrid functional was previously calibrated versus QMC results for the cuprate spin, charge, and phonon behavior [51]. The pseudopotentials by Burkatzki, Filippi, and Dolg [52,53] were used to remove core electrons. The wave functions were represented by the triple-ζ basis set included with those potentials. A k-point mesh of $4 \times 4 \times 4$ was used to integrate over the Brillouin zone according to a Pack-Monkhorst sampling. The optimized lattice parameters for the AF configuration of the ORTH structure are given by $a = 5.182$ Å, $b = 5.347$ Å, and $c = 24.47$ Å. Phonon frequency calculations were performed using a frozen phonon approach at $\vec{q} = (0, 0, 0)$ and $(1, 1, 0)$.

For phonon band structure simulations with dispersion corrected functionals, DFT with projector-augmented wave pseudopotentials was employed as implemented in the Vienna *ab initio* simulation package (VASP) code [54–57]. Van der Waals dispersions between Bi-O layers are accounted for by utilizing the rev-vdW-DF2 functional [48], which has been shown to be relatively accurate in calculating interlayer and intralayer lattice constants in layered solids [58]. The on-site Coulomb repulsion U was set to 6 eV for the Cu 3d orbitals in the system. This value is in accordance with the broader range of Hubbard U values (ranging from $U = 4$ eV to $U = 8$ eV) employed in the literature for investigating various aspects of Cuprate electronic structure [59–63], with $U = 6$ eV specifically utilized by Bellini *et al.* in studying the Fermi surface of bismuth-based cuprates [61]. In consideration of the incommensurate Bi-O modulations in the real system [42], the vdW DFT simulations investigated two antiferromagnetic configurations based on the ORTH structure with modified Bi-O bonding environments as shown in Fig. 9. The first structure (termed "XY") in Fig. 9(a) has been modified to exhibit Bi-O intralayer dimerization along both the *a*- and *b*-lattice directions instead of only along the *b*-lattice direction present in the ORTH structure. The second considered struc-
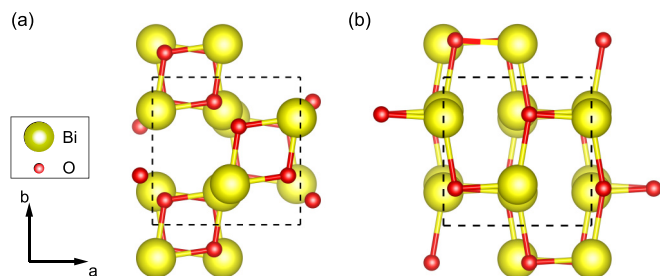
FIG. 9. Top view of the (a) Bi-O layers for XY structure and (b) zigzag structure of Bi2201.
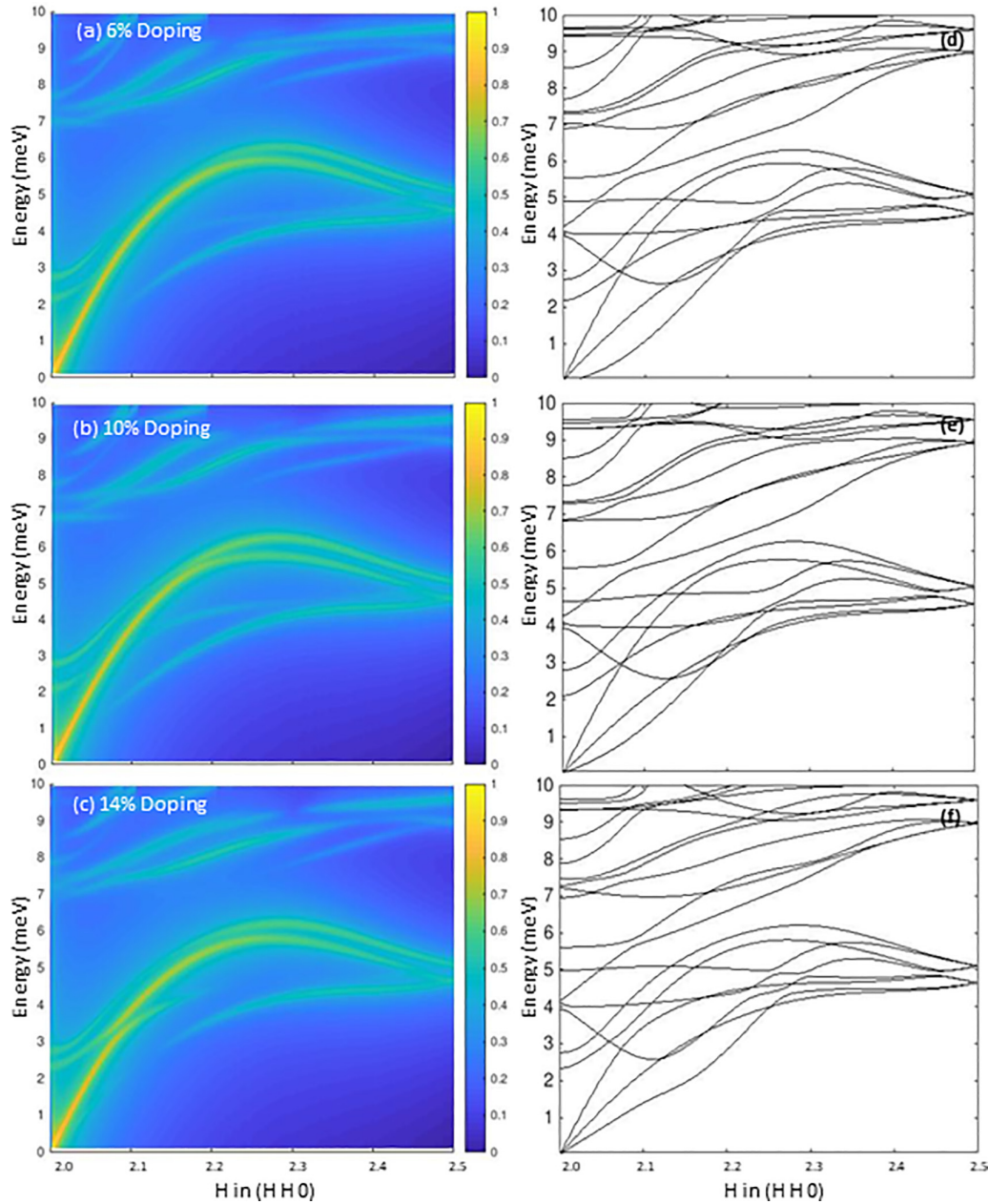
FIG. 10. Theoretical doping dependence of phonons for Bi2201 using the rev-vdW-DF2 functional on the Bi-O zigzag structure. Simulated IXS spectra along the (H H 0) direction for (a) 6% doping, (b) 10% doping, and (c) 14% doping. (d)–(f) Calculated phonon dispersions for 6%, 10%, and 14% doping, respectively. Intensities have been normalized and plotted on a logarithmic scale for clarity. All systems are in the stable antiferromagnetic state and predicted no unstable phonon modes.

ture in Fig. 9(b) follows from the results of Nokelainen *et al.* who used the SCAN functional to determine a Bi-O bonding configuration of stacking zigzag chains in Bi2212 [64]. Both variations were modified starting from the ORTH structure of Torardi *et al.* [42] obtained from the ICSD [65].

Geometry optimizations of the initial structure were performed by relaxing all degrees of freedom until the Hellman-Feynman forces were less than $0.001 \, \text{eV/Å}$ with a $6 \times 6 \times 1$ Γ-centered k-point sampling mesh and a plane wave cutoff energy of 520 eV. Table I summarizes the final relaxed lattice constants for the investigated systems using these parameters. Phonon dispersions were calculated using the PHONOPY package [47] with a $2 \times 2 \times 1$ supercell (176

total atoms) and a $3 \times 3 \times 1$ k-point mesh. To qualitatively reproduce the trends seen experimentally with doping dependence of the low-energy phonons, we consider three different hole doping levels —0% (undoped), 12%, and 20% doping— through the virtual crystal approximation [66]. In this way, Pb doping is effectively introduced into the system by modifying the Bi nuclear charge to be the average of the Bi and Pb nuclear charges. Similarly, three doping levels of 6%, 10%, and 14% were analyzed for the zigzag bonding structure. For each motif (XY or zigzag), the doping levels were chosen from a doping range in which the optimized structures present a minimum number of unstable phonon modes. We also note that in the range of investigated dopings, the AF configuration

TABLE III. Comparison of experimental and calculated lattice constants (in Å) for hole-doped Bi2201 systems. Calculated constants are obtained with the rev-vdW-DF2 functional on the Bi-O zigzag structure.

	Experiment			Calculated		
	AF	UD15K	OD11K	6%	10%	14%
a	5.436	5.4	5.4	5.3038	5.3028	5.292
b	5.502	5.445	5.308	5.4028	5.4080	5.406
c	23.91	24.34	24.56	24.5535	24.5568	24.5571

remained magnetically stable relative to a ferromagnetic one. An analysis of other modulated magnetic orderings, such as stripes, which require larger supercells, is beyond the scope of this study. Simulated IXS spectra were made using the SNAXS software package [67]. Structures were visualized with VESTA [27].

APPENDIX C: PHONON CALCULATIONS FOR BI-O ZIGZAG ORTH STRUCTURE

Figure 10 shows the simulated IXS and calculated dispersions of three hole doping levels using the Bi-O zigzag bonding structure as shown in Fig. 9(b). The hole doping levels were chosen such that no phonon mode instabilities were predicted within the presented doping range, thus allowing for the IXS simulations to be performed along the experimentally observed (220) direction. We note that the vdW modes have low intensity in this structure and we hypothesize the dimerization motif represented by our XY structure is responsible for the IXS intensity of the vdW modes. This is further supported by the reduced c-lattice expansion in the zigzag bond configuration (Table III).
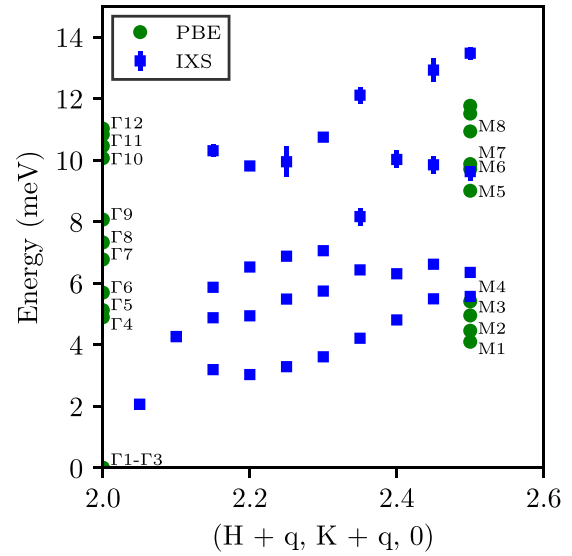
FIG. 12. Theoretical and experimental phonon modes. The theoretical phonons were computed using DFT in the PBE approximation.

APPENDIX D: PBE CALCULATIONS FOR THE PHONONS

The PBE functional was also investigated. This approximation, however, did not converge to the starting antiferromagnetic ordering, which is a common issue in cuprate materials [68]. For this reason, most of the analysis and discussion in this work are done in the PBE0 functional. Nevertheless, the phonon frequencies in the PBE approximation are reported in Table II. The diagram of phonon eigenvectors is displayed in Fig. 11, and the phonon frequencies in the PBE approximation are plotted in Fig. 12. The M1 mode is
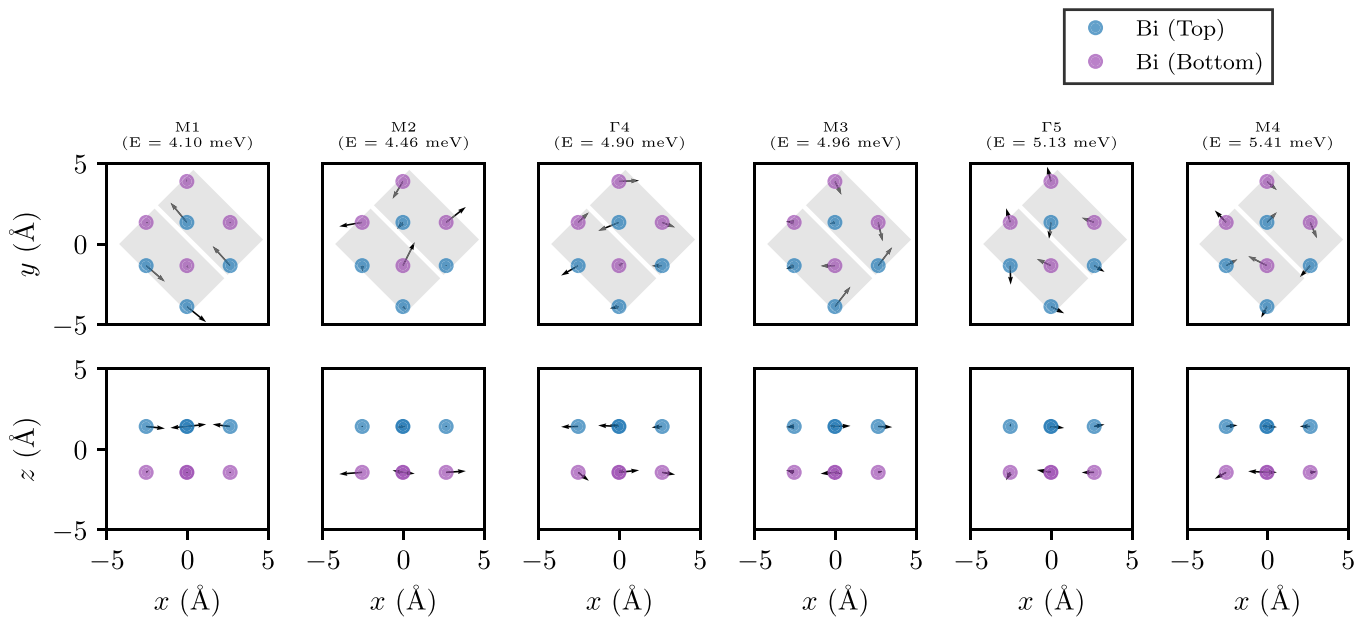
FIG. 11. Phonon eigenvectors from DFT (PBE) calculations. Oxygen atoms are not included in the plots to clearly visualize the displacement of Bi atoms. Each column displays a phonon mode, with the top layer showing the top-down view and the bottom layer showing the side view.

associated with only the Bi atoms in the top plane moving horizontally, while the M2 mode shows only the Bi atoms in the bottom plane moving. The Bi planes are decoupled as shown in the bottom panels of Fig. 11.

---

[1] K. S. Novoselov, A. Mishchenko, A. Carvalho, and A. H. C. Neto, 2D materials and van der Waals heterostructures, Science **353**, aac9439 (2016).

[2] J. A. Wilson and A. D. Yoffe, The transition metal dichalcogenides discussion and interpretation of the observed optical, electrical and structural properties, Adv. Phys. **18**, 193 (1969).

[3] R. Fivaz and E. Mooser, Electron-phonon interaction in semiconducting layer structures, Phys. Rev. **136**, A833 (1964).

[4] B. Keimer, S. A. Kivelson, M. R. Norman, S. Uchida, and J. Zaanen, From quantum matter to high-temperature superconductivity in copper oxides, Nature (London) **518**, 179 (2015).

[5] Y. Cao, V. Fatemi, A. Demir, S. Fang, S. L. Tomarken, J. Y. Luo, J. D. Sanchez-Yamagishi, K. Watanabe, T. Taniguchi, E. Kaxiras, R. C. Ashoori, and P. Jarillo-Herrero, Correlated insulator behaviour at half-filling in magic-angle graphene superlattices, Nature (London) **556**, 80 (2018).

[6] Y. Jiang, X. Lai, K. Watanabe, T. Taniguchi, K. Haule, J. Mao, and E. Y. Andrei, Charge order and broken rotational symmetry in magic-angle twisted bilayer graphene, Nature (London) **573**, 91 (2019).

[7] Y. Cao, D. Chowdhury, D. Rodan-Legrain, O. Rubies-Bigorda, K. Watanabe, T. Taniguchi, T. Senthil, and P. Jarillo-Herrero, Strange metal in magic-angle graphene with near planckian dissipation, Phys. Rev. Lett. **124**, 076801 (2020).

[8] E. Y. Andrei and A. H. MacDonald, Graphene bilayers with a twist, Nature Mater. **19**, 1265 (2020).

[9] G. Fiori, F. Bonaccorso, G. Iannaccone, T. Palacios, D. Neumaier, A. Seabaugh, S. K. Banerjee, and L. Colombo, Electronics based on two-dimensional materials, Nature Nanotechnol. **9**, 768 (2014).

[10] Y. Y. Peng, J. Q. Meng, D. X. Mou, J. F. He, L. Zhao, Y. Wu, G. D. Liu, X. L. Dong, S. L. He, J. Zhang, X. Y. Wang, Q. J. Peng, Z. M. Wang, S. J. Zhang, F. Yang, C. T. Chen, Z. Y. Xu, T. K. Lee, and X. J. Zhou, Disappearance of nodal gap across the insulator–superconductor transition in a copper-oxide superconductor, Nature Commun. **4**, 2459 (2013).

[11] R. Comin, A. Frano, M. M. Yee, Y. Yoshida, H. Eisaki, E. Schierle, E. Weschke, R. Sutarto, F. He, A. Soumyanarayanan, Y. He, M. L. Tacon, I. Elfimov, J. E. Hoffman, G. Sawatzky, B. Keimer, and A. Damascelli, Charge order driven by Fermi-arc instability in $Bi_2Sr_{2-x}La_xCuO_{6+\delta}$, Science **343**, 390 (2014).

[12] M. L. Tacon, A. Bosak, S. Souliou, G. Dellea, T. Loew, R. Heid, K. Bohnen, G. Ghiringhelli, M. Krisch, and B. Keimer, Inelastic X-ray scattering in $YBa_2Cu_3O_{6.6}$ reveals giant phonon anomalies and elastic central peak due to charge-density-wave formation, Nature Phys. **10**, 52 (2014).

[13] H. Miao, D. Ishikawa, R. Heid, M. Le Tacon, G. Fabbris, D. Meyers, G. D. Gu, A. Q. R. Baron, and M. P. M. Dean, Incommensurate phonon anomaly and the nature of charge density waves in cuprates, Phys. Rev. X **8**, 011008 (2018).

[14] Y. He, S. Wu, Y. Song, W.-S. Lee, A. H. Said, A. Alatas, A. Bosak, A. Girard, S. M. Souliou, A. Ruiz, M. Hepting, M. Bluschke, E. Schierle, E. Weschke, J.-S. Lee, H. Jang, H. Huang, M. Hashimoto, D.-H. Lu, D. Song *et al.*, Persistent low-energy phonon broadening near the charge-order *q* vector in the bilayer cuprate $Bi_2Sr_2CaCu_2O_{8+\delta}$, Phys. Rev. B **98**, 035102 (2018).

[15] J. Li, A. Nag, J. Pelliciari, H. Robarts, A. Walters, M. Garcia-Fernandez, H. Eisaki, D. Song, H. Ding, S. Johnston, R. Comin, and K.-J. Zhou, Multiorbital charge-density wave excitations and concomitant phonon anomalies in $Bi_2Sr_2LaCuO_{6+\delta}$, Proc. Natl. Acad. Sci. USA **117**, 16219 (2020).

[16] R. Arpaia and G. Ghiringhelli, Charge order at high temperature in cuprate superconductors, J. Phys. Soc. Jpn. **90**, 111005 (2021).

[17] A. Frano, S. Blanco-Canosa, B. Keimer, and R. J. Birgeneau, Charge ordering in superconducting copper oxides, J. Phys.: Condens. Matter **32**, 374005 (2020).

[18] H. Sinn, Spectroscopy with meV energy resolution, J. Phys.: Condens. Matter **13**, 7525 (2001).

[19] E. Burkel, Phonon spectroscopy by inelastic x-ray scattering, Rep. Prog. Phys. **63**, 171 (2000).

[20] P. Hohenberg and W. Kohn, Inhomogeneous electron gas, Phys. Rev. **136**, B864 (1964).

[21] W. Kohn and L. J. Sham, Self-consistent equations including exchange and correlation effects, Phys. Rev. **140**, A1133 (1965).

[22] P. H. Tan, W. P. Han, W. J. Zhao, Z. H. Wu, K. Chang, H.Wang, Y. F.Wang, N. Bonini, N. Marzari, N. Pugno, G. Savini, A. Lombardo, and A. C. Ferrari, The shear mode of multilayer graphene, Nature Mater. **11**, 294 (2012).

[23] Y. Zhao, X. Luo, H. Li, J. Zhang, P. T. Araujo, C. K. Gan, J. Wu, H. Zhang, S. Y. Quek, M. S. Dresselhaus, and Q. Xiong, Interlayer breathing and shear modes in few-trilayer MoS_2 and WSe_2, Nano Lett. **13**, 1007 (2013).

[24] L. Zhao, W. T. Zhang, H. Y. Liu, J. Q. Meng, G. D. Liu, W. Lu, X. L. Dong, and X. J. Zhou, High-quality large-sized single crystals of Pb-Doped $Bi_2Sr_2CuO_{6+\delta}$ High-T_c superconductors grown with traveling solvent floating zone method, Chin. Phys. Lett. **27**, 087401 (2010).

[25] A. H. Said, H. Sinn, T. S. Toellner, E. E. Alp, T. Gog, B. M. Leu, S. Bean, and A. Alatas, High-energy-resolution inelastic X-ray scattering spectrometer at beamline 30-ID of the Advanced Photon Source, J. Synchrotron Radiat. **27**, 827 (2020).

[26] T. S. Toellner, A. Alatas, and A. H. Said, Six-reflection meV-monochromator for synchrotron radiation, J. Synchrotron Radiat. **18**, 605 (2011).

[27] K. Momma and F. Izumi, *VESTA3* for three-dimensional visualization of crystal, volumetric and morphology data, J. Appl. Crystallogr. **44**, 1272 (2011).

[28] Z. Chen, Y. Y. Peng, Z. Wang, Y. J. Song, J. Q. Meng, X. J. Zhou, and J. Q. Li, Compositional evolution of the antiphase stripe superstructure in $Bi_2Sr_{2-x}La_xCuO_6$ ($0 < x \leqslant 1.1$) revealed by transmission electron microscopy, Supercond. Sci. Technol. **26**, 055010 (2013).

[29] J. Chang, E. Blackburn, A. T. Holmes, N. B. Christensen, J. Larsen, J. Mesot, R. Liang, D. A. Bonn, W. N. Hardy, A. Watenphul, M. v. Zimmermann, E. M. Forgan, and S. M.

Hayden, Direct observation of competition between superconductivity and charge density wave order in $YBa_2Cu_3O_{6.67}$, Nature Phys. **8**, 871 (2012).

[30] R. Arpaia, S. Caprara, R. Fumagalli, G. D. Vecchi, Y. Y. Peng, E. Andersson, D. Betto, G. M. D. Luca, N. B. Brookes, F. Lombardi, M. Salluzzo, L. Braicovich, C. D. Castro, M. Grilli, and G. Ghiringhelli, Dynamical charge density fluctuations pervading the phase diagram of a Cu-based high-T_c superconductor, Science **365**, 906 (2019).

[31] Y. Y. Peng, M. Salluzzo, X. Sun, A. Ponti, D. Betto, A. M. Ferretti, F. Fumagalli, K. Kummer, M. Le Tacon, X. J. Zhou, N. B. Brookes, L. Braicovich, and G. Ghiringhelli, Direct observation of charge order in underdoped and optimally doped $Bi_2(Sr, La)_2CuO_{6+\delta}$ by resonant inelastic x-ray scattering, Phys. Rev. B **94**, 184511 (2016).

[32] S. L. Chaplot, W. Reichardt, L. Pintschovius, and N. Pyka, Common interatomic potential model for the lattice dynamics of several cuprates, Phys. Rev. B **52**, 7230 (1995).

[33] C. J. Bonnoit, Ph.D. thesis, Massachusetts Institute of Technology, 2013.

[34] S. K. Sinha, Theory of inelastic x-ray scattering from condensed matter, J. Phys.: Condens. Matter **13**, 7511 (2001).

[35] K. Kurashima, T. Adachi, K. M. Suzuki, Y. Fukunaga, T. Kawamata, T. Noji, H. Miyasaka, I. Watanabe, M. Miyazaki, A. Koda, R. Kadono, and Y. Koike, Development of ferromagnetic fluctuations in heavily overdoped $(Bi, Pb)_2Sr_2CuO_{6+\delta}$ copper oxides, Phys. Rev. Lett. **121**, 057002 (2018).

[36] W. Fan and Z. Zeng, The modulation and reconstruction of a BiO layer of cuprate bi2212, Supercond. Sci. Technol. **24**, 105007 (2011).

[37] O. Can, T. Tummuru, R. P. Day, I. Elfimov, A. Damascelli, and M. Franz, High-temperature topological superconductivity in twisted double-layer copper oxides, Nature Phys. **17**, 519 (2021).

[38] Q. Li, Y. N. Tsay, M. Suenaga, R. A. Klemm, G. D. Gu, and N. Koshizuka, $Bi_2Sr_2CaCu_2O_{8+\delta}$ bicrystal c-axis twist Josephson junctions: A new phase-sensitive test of order parameter symmetry, Phys. Rev. Lett. **83**, 4160 (1999).

[39] Y. Zhu, M. Liao, Q. Zhang, H.-Y. Xie, F. Meng, Y. Liu, Z. Bai, S. Ji, J. Zhang, K. Jiang, R. Zhong, J. Schneeloch, G. Gu, L. Gu, X. Ma, D. Zhang, and Q.-K. Xue, Presence of s-wave pairing in josephson junctions made of twisted ultrathin $Bi_2Sr_2CaCu_2O_{8+x}$ flakes, Phys. Rev. X **11**, 031011 (2021).

[40] H. Heinrich, G. Kostorz, B. Heeb, and L. Gauckler, Modelling the atomic displacements in $Bi_2Sr_2Ca_{n-1}Cu_nO_x$ superconductors, Physica C: Superconductivity **224**, 133 (1994).

[41] D. J. Singh and W. E. Pickett, Structural modifications in bismuth cuprates: Effects on the electronic structure and fermi surface, Phys. Rev. B **51**, 3128 (1995).

[42] C. C. Torardi, M. A. Subramanian, J. C. Calabrese, J. Gopalakrishnan, E. M. McCarron, K. J. Morrissey, T. R. Askew, R. B. Flippen, U. Chowdhry, and A. W. Sleight, Structures of the superconducting oxides $Tl_2Ba_2CuO_6$ and $Bi_2Sr_2CuO_6$, Phys. Rev. B **38**, 225 (1988).

[43] R. Dovesi, R. Orlando, B. Civalleri, C. Roetti, V. R. Saunders, and C. M. Zicovich-Wilson, Crystal: a computational tool for the *ab initio* study of the electronic properties of crystals, Z. Kristallogr. **220**, 571 (2005).

[44] R. Dovesi, V. R. Saunders, C. Roetti, R. Orlando, C. Zicovich-Wilson, F. Pascale, B. Civalleri, K. Doll, N. M. Harrison, I. J. Bush *et al.*, CRYSTAL09, User's Manual: Torino, Italy, 2009.

[45] G. Kresse, J. Furthmüller, and J. Hafner, *Ab initio* force constant approach to phonon dispersion relations of diamond and graphite, Europhys. Lett. **32**, 729 (1995).

[46] K. Parlinski, Z. Q. Li, and Y. Kawazoe, First-principles determination of the soft mode in cubic ZrO_2, Phys. Rev. Lett. **78**, 4063 (1997).

[47] A. Togo and I. Tanaka, First principles phonon calculations in materials science, Scr. Mater. **108**, 1 (2015).

[48] I. Hamada, van der waals density functional made accurate, Phys. Rev. B **89**, 121103(R) (2014).

[49] J. P. Perdew, K. Burke, and M. Ernzerhof, Generalized gradient approximation made simple, Phys. Rev. Lett. **77**, 3865 (1996).

[50] C. Adamo and V. Barone, Toward reliable density functional methods without adjustable parameters: The PBE0 model, J. Chem. Phys. **110**, 6158 (1999).

[51] L. K. Wagner and P. Abbamonte, Effect of electron correlation on the electronic structure and spin-lattice coupling of high-T_c cuprates: Quantum monte carlo calculations, Phys. Rev. B **90**, 125129 (2014).

[52] M. Burkatzki, C. Filippi, and M. Dolg, Energy-consistent pseudopotentials for quantum monte carlo calculations, J. Chem. Phys. **126**, 234105 (2007).

[53] M. Burkatzki, C. Filippi, and M. Dolg, Energy-consistent small-core pseudopotentials for $3d$-transition metals adapted to quantum Monte Carlo calculations, J. Chem. Phys. **129**, 164115 (2008).

[54] G. Kresse and J. Hafner, *Ab initio* molecular dynamics for liquid metals, Phys. Rev. B **47**, 558 (1993).

[55] G. Kresse and J. Hafner, *Ab initio* molecular-dynamics simulation of the liquid-metal–amorphous-semiconductor transition in germanium, Phys. Rev. B **49**, 14251 (1994).

[56] G. Kresse and J. Furthmüller, Efficiency of *ab-initio* total energy calculations for metals and semiconductors using a plane-wave basis set, Comput. Mater. Sci. **6**, 15 (1996).

[57] G. Kresse and J. Furthmüller, Efficient iterative schemes for *ab initio* total-energy calculations using a plane-wave basis set, Phys. Rev. B **54**, 11169 (1996).

[58] F. Tran, L. Kalantari, B. Traoré, X. Rocquefelte, and P. Blaha, Nonlocal van der waals functionals for solids: Choosing an appropriate one, Phys. Rev. Mater. **3**, 063602 (2019).

[59] V. I. Anisimov, M. A. Korotin, A. S. Mylnikova, A. V. Kozhevnikov, D. M. Korotin, and J. Lorenzana, Computation of stripes in cuprates within the LDA + U method, Phys. Rev. B **70**, 172501 (2004).

[60] H. Eschrig, K. Koepernik, and I. Chaplygin, Density functional application to strongly correlated electron systems, J. Solid State Chem. **176**, 482 (2003).

[61] V. Bellini, C. Rozzi, and F. Manghi, Correlation effects on the electronic properties of $Bi_2Sr_2CaCu_2O_8$, J. Phys. Chem. Solids **67**, 286 (2006).

[62] M. S. Hybertsen, E. B. Stechel, M. Schluter, and D. R. Jennison, Renormalization from density-functional theory to strong-coupling models for electronic states in Cu-O materials, Phys. Rev. B **41**, 11068 (1990).

[63] S. Pesant and M. Côté, DFT $+U$ study of magnetic order in doped La_2CuO_4 crystals, Phys. Rev. B **84**, 085104 (2011).

[64] J. Nokelainen, C. Lane, R. S. Markiewicz, B. Barbiellini, A. Pulkkinen, B. Singh, J. Sun, K. Pussi, and A. Bansil, *Ab initio* description of the $bi_2sr_2cacu_2o_{8+\delta}$ electronic structure, Phys. Rev. B **101**, 214523 (2020).

[65] A. Belsky, M. Hellenbrandt, V. L. Karen, and P. Luksch, New developments in the Inorganic Crystal Structure Database (ICSD): accessibility in support of materials research and design, Acta Crystallogr. Sect. B **58**, 364 (2002).

[66] O. Sinai and L. Kronik, Simulated doping of si from first principles using pseudoatoms, Phys. Rev. B **87**, 235305 (2013).

[67] D. Parshall, https://github.com/danparshall/snaxs.

[68] M. K. Horton, J. H. Montoya, M. Liu, and K. A. Persson, High-throughput prediction of the ground-state collinear magnetic order of inorganic materials using density functional theory, npj Comput. Mater. **5**, 64 (2019).